




Symmetry-driven embedding of networks in hyperbolic space

Simon Lizotte ^{1,2}, Jean-Gabriel Young ^{1,3,4} and Antoine Allard ^{1,2,4}

¹*Département de physique, de génie physique et d'optique,
Université Laval, Québec (Québec), Canada G1V 0A6*

²*Centre interdisciplinaire en modélisation mathématique,
Université Laval, Québec (Québec), Canada G1V 0A6*

³*Department of Mathematics and Statistics, University of Vermont, Burlington, VT 05405, USA*

⁴*Vermont Complex Systems Center, University of Vermont, Burlington, VT 05405, USA*

Hyperbolic models can reproduce the heavy-tailed degree distribution, high clustering, and hierarchical structure of empirical networks. Current algorithms for finding the hyperbolic coordinates of networks, however, do not quantify uncertainty in the inferred coordinates. We present BIGUE, a Markov chain Monte Carlo (MCMC) algorithm that samples the posterior distribution of a Bayesian hyperbolic random graph model. We show that combining random walk and random cluster transformations significantly improves mixing compared to the commonly used and state-of-the-art dynamic Hamiltonian Monte Carlo algorithm. Using this algorithm, we also provide evidence that the posterior distribution cannot be approximated by a multivariate normal distribution, thereby justifying the use of MCMC to quantify the uncertainty of the inferred parameters.

I. INTRODUCTION

Embedding enables us to comprehend abstract objects and conduct rigorous quantitative analyses of their similarities, differences, and structural characteristics. In the complex network context, embeddings usually consist of node coordinates in a latent space. A rich literature has shown that embedding in hyperbolic spaces [1], in particular, can visually emphasize the important parts of large networks [2], but also, when used as the basis for a random graph model, naturally reproduce many common network properties such as the community structure [3–7], a power-law degree distribution [8, 9], a non-vanishing clustering coefficient [8–12], a fractal structure [13–15] and the sparsity of connections [12]. Furthermore, since hyperbolic geometry closely approximate the shortest paths of graphs via geodesics [8, 16], hyperbolic embeddings have been used to design efficient routing protocols [17, 18].

Considerable effort has gone into representing a given graph using latent spaces [19–23]. Many studies focus on placing the vertices such that the graph distance between the vertices is closely approximated by the hyperbolic geodesics [24–28]. From this perspective, Ref. [29] proved that trees can be embedded in hyperbolic space up to an arbitrarily small error, enabling perfect greedy routing. This is due to the exponentially growing volume in the hyperbolic space, which can be related to the branching factor of trees [8]. The embedding task was also tackled with dimension reduction techniques from machine learning [23, 30–32] and with the maximum likelihood estimation of various hyperbolic random graph models [17, 33–42]. Other methods allow the embedding of directed graphs [43–45], weighted graphs [46, 47] and graphs to the D -dimensional hyperbolic space with [48] or without vertex features [49].

Existing methods have largely overlooked uncertainty: They return a single embedding without allowance for error or multimodality. Yet, this information is crucial as

perturbations to the embedding affect link prediction [50] and can lead to different graph representations. As a first step towards addressing this problem, we present BIGUE (Bayesian Inference of a Graph’s Unknown Embedding), a Markov chain Monte Carlo (MCMC) algorithm that samples the posterior distribution of a Bayesian model constructed from the commonly used \mathbb{H}^2 hyperbolic random graph model (HRGM); see Fig. 1.

The Bayesian hyperbolic embedding of networks has already been studied in Ref [51], but the results therein suggest that the proposed MCMC algorithm has poor mixing—a common problem for many standard and state-of-the-art MCMC methods when the posterior distribution is complex and multimodal [52–60]. We identify community structure [61] as a source of multimodal-

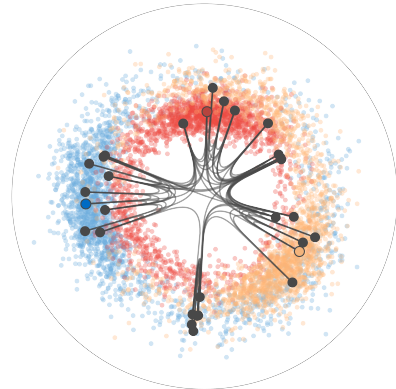


FIG. 1. Probabilistic hyperbolic embedding of a synthetic graph with BIGUE. Hyperbolic coordinates are obtained using a transformation between the \mathbb{H}^2 and the \mathbb{S}^1 models described in Appendix A. Black points and dark-colored points are the median coordinates of each vertex. Light-colored points are sampled positions for the three highlighted vertices. Lines are edges drawn using hyperbolic geodesics. We used 2,000 samples corresponding to the simulations shown in Fig. 3d.

ity and introduce a set of cluster-based transformations to improve the exploration of the posterior distribution. Our approach draws on previous literature in which community structure was used to guide greedy embedding algorithms [41, 62]. We show that these transformations drastically improve the mixing of the MCMC algorithm, allowing us to find appropriate credible intervals for the parameters of the HRGM and any graph property. We also show that multimodality can be induced in the posterior by having a vertex with two positions and that it is identified by BIGUE.

II. BAYESIAN HYPERBOLIC EMBEDDING

A. Model definition

Let \mathcal{G} be a random graph and $G = (V, E)$ be the graph we aim to embed. We use the circular probabilistic model \mathbb{S}^1 to describe the graph G ; it is nearly equivalent to the hyperbolic plane model \mathbb{H}^2 [8] (see Appendix A), but it will turn out to facilitate inference. In the \mathbb{S}^1 model, the probability that an edge (u, v) exists between vertices u and v is a function of the angular coordinates $\theta = (\theta_w)_{w \in V}$ of the vertices where each $\theta_w \in [-\pi, \pi)$, of the parameters $\kappa = (\kappa_w)_{w \in V}$ where each $\kappa_w > 0$ control the degree of vertices, and of an inverse temperature $\beta > 1$ which controls the amount of clustering. This probability is defined as

$$\mathbb{P}[(u, v) \in E | \theta, \kappa, \beta] = \left(1 + \left(\frac{d(\theta_u, \theta_v)}{\mu \kappa_u \kappa_v} \right)^\beta \right)^{-1}, \quad (1)$$

where $d(\theta_u, \theta_v) = R\Delta(\theta_u, \theta_v)$ is the arc length between vertices u and v , $\Delta(\theta_u, \theta_v) = \pi - |\pi - |\theta_u - \theta_v||$ is the angular separation, and $R = |V|/2\pi$ is the radius of the circle on which vertices are embedded. We fix the constant $\mu = \beta \sin(\pi/\beta)/2\pi\mathbb{E}[\kappa]$ so that the parameters κ match the degrees $\mathbb{E}[K(\kappa)] = \kappa$ in expectation in the limit of large graphs, where $K(\kappa)$ is the random degree of a vertex of parameter κ when all vertices are independently and uniformly distributed on the circle [8].

The complete graph is modeled using conditional independence for the edges, leading to the likelihood

$$\begin{aligned} \mathbb{P}[\mathcal{G} = G | \theta, \kappa, \beta] &= \prod_{(u, v) \in E} \mathbb{P}[(u, v) \in E | \theta, \kappa, \beta] \\ &\quad \times \prod_{(u, v) \notin E} (1 - \mathbb{P}[(u, v) \in E | \theta, \kappa, \beta]) \\ &= \prod_{(u, v) \in \binom{V}{2}} \left(1 + \left(\frac{d(\theta_u, \theta_v)}{\mu \kappa_u \kappa_v} \right)^{\beta_{uv}^\pm} \right)^{-1}, \end{aligned} \quad (2)$$

where $\binom{V}{2}$ is the set of all combinations of two vertices and β_{uv}^\pm is β if $(u, v) \in E$ and is $-\beta$ otherwise.

Applying Bayes' rule yields the following posterior density for the embedding (i.e., angular coordinates and parameters)

$$p(\theta, \kappa, \beta | G) = \frac{\mathbb{P}[\mathcal{G} = G | \theta, \kappa, \beta] p(\theta, \kappa, \beta)}{\mathbb{P}[\mathcal{G} = G]}. \quad (3)$$

The likelihood $\mathbb{P}[\mathcal{G} = G | \theta, \kappa, \beta]$ is given by Eq. (2). To complete the specification of Eq. (3), we use independent prior densities

$$p(\theta, \kappa, \beta) = p(\beta) \prod_{w \in V} p(k_w) p(\theta_w), \quad (4)$$

for ease of modeling, though our sampling algorithm does not depend on this simplifying assumption. Previous literature has shown that inverse temperatures are typically small; we thus choose a truncated half-normal distribution for β ,

$$p(\beta) \propto \mathbb{1}[\beta > 1] \exp\left\{ -\frac{(\beta - \beta_0)^2}{2\sigma^2} \right\} \quad (5)$$

with $\beta_0 = 3$ and $\sigma = 2$. Since known networks tend to have a heavy-tailed degree distribution, we use a half-Cauchy prior

$$p(\kappa_w) \propto \mathbb{1}[\kappa_w > \varepsilon] \frac{2}{\pi\gamma(1 + (\kappa_w/\gamma)^2)}, \quad \forall w \in V \quad (6)$$

with $\gamma = 4$ and $\varepsilon = 10^{-10}$; this allows for large variations in the estimated values of κ . Finally, because the angular coordinates are defined on a bounded space and we do not want to favor an embedding direction *a priori*, we use a uniform prior

$$p(\theta_w) = \frac{1}{2\pi} \quad (7)$$

except for the two vertices with the highest degree, whose position is fixed (the reason is technical and has to do with avoiding degeneracy in the posterior; see below.) With these choices, the posterior distribution is proper and can express correlations between the parameters even if the priors are independent. The normalization constant $\mathbb{P}[\mathcal{G} = G]$ can be contained by integration in principle, though it is not needed here; see Sec. III below.

B. Symmetries and automorphisms

Our Bayesian approach to hyperbolic embedding exacerbates two definitional issues that are usually ignored when the model is used with maximization algorithms.

First, the model inherits the symmetries of the circle \mathbb{S}^1 . Since the distance d is invariant to rotations and reflections $\theta_w \mapsto -\theta_w$, the edge probabilities are preserved in the likelihood, and an infinite number of equivalent embeddings exist. Maximization algorithms break this symmetry at random, but we need to proceed with more

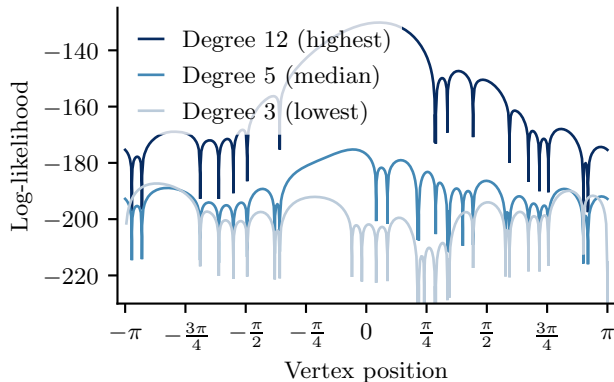


FIG. 2. Log-likelihood of the model when a single vertex is moved along the circle. Each dip is a divergence that occurs when a vertex is positioned at the same position as a non-adjacent vertex. These divergences form barriers in the objective function landscape (log-likelihood, posterior distribution), which is one of the reasons why hyperbolic embedding is a difficult problem.

caution when we move to a distribution over embedding. Without loss of generality, we fix the angular coordinate of the highest-degree vertex u to $\theta_u = 0$ to handle rotational symmetries. We remove the reflection symmetry by restricting the angular coordinate of the second highest-degree vertex v to $\theta_v \in [0, \pi)$.

Second, a graph is inherently labeled by its vertices, but any vertex relabelling that preserves the edges—an *automorphism*—leaves the likelihood invariant since the distances between connected and unconnected vertices are unchanged. For example, if a transformation $u \leftrightarrow v$ exists such that each $(u, w) \in E \implies (v, w) \in E$ and $(v, w) \in E \implies (u, v) \in E$, then we can also exchange $k_u \leftrightarrow k_v$ and $\theta_u \leftrightarrow \theta_v$ in the likelihood. We account for this symmetry by defining the likelihood up to an automorphism.

III. SAMPLING

The posterior density, Eq. (3), does not correspond to the closed-form density of a known distribution, and computing analytical expectations thus appears difficult. Therefore, we turn to numerical estimates with sampling.

Unfortunately, for most graphs G , the posterior distribution has a complicated geometry, making the application of well-known sampling algorithms challenging. This is the case even for small graphs, as Fig. 2 shows: changing the embedding coordinates of a single vertex reveals multiple local maxima of the likelihood (and thus posterior density) for a small graph of 30 vertices. The model predicts that two vertices with nearby embedding coordinates should be connected with high probability. In the extreme case where non-adjacent vertices have the same angular coordinate, the likelihood approaches 0, causing

the sharp dips shown in the Figure. Further, the gradients are undefined due to their dependence on the distance function in Eq. (1). Since the posterior geometry is filled with these barriers for sparse and large graphs (the number of modes increases with the number of non-adjacent pairs of vertices), hyperbolic embedding can be challenging for standard algorithms.

A. Baseline algorithms

To understand how standard algorithms fare with such a complex posterior distribution, we first tested a naive random walk MCMC (RW) algorithm (details in Appendix C) on a small synthetic graph with known ground truth embedding coordinates (shown in Fig. 1). We quantified our results using the autocorrelation, the effective number of samples n_{eff} , and \hat{R} —a measure of mixing (see Appendix D for details). Further, we tested convergence by initializing the algorithm (i) at the ground truth and (ii) with a simple initialization strategy that can be applied to observational data. Figure 3 illustrates that although the RW has a high autocorrelation, it very slowly reaches the typical set—the part of the distribution that holds a significant probability mass and where good algorithms should naturally spend most of its time [63].

For our second test, we wrote the model in Stan, a probabilistic programming language that implements a state-of-the-art dynamic Hamiltonian Monte Carlo (HMC) algorithm [64] for sampling from arbitrary Bayesian models. Dynamic HMC runs slowly because each sampling step involves integrating a large system of differential equations. Nonetheless, the promise of high-quality samples makes this option worth exploring.

Unfortunately, the barriers shown in Fig 2 are problematic for a purely gradient-based method such as HMC, and Stan indeed reports gradient divergences, which signal incorrect sampling. This issue can be partially mitigated by using an approximate likelihood (described in Appendix B) that smoothens these barriers at the cost of a slightly distorted posterior. However, even with this modification, the algorithm is unable to explore the sampling space sufficiently fast (we reach the maximum tree depth easily [64]).

Stan’s default parameters can be modified to allow for better exploration (increased tree depth), but even then, a critical problem remains and seems insurmountable: after a large number of iterations, the sampled distribution differs depending on the initialization, a signal that the mixing is poor; see Fig. 3. Initializations at the ground truth yield high-quality samples, but random initializations do not converge to the typical set even after 200,000 iterations. This mixing issue is likely caused by the complicated and non-convex geometry of the posterior distribution, which motivates the modifications we propose next.

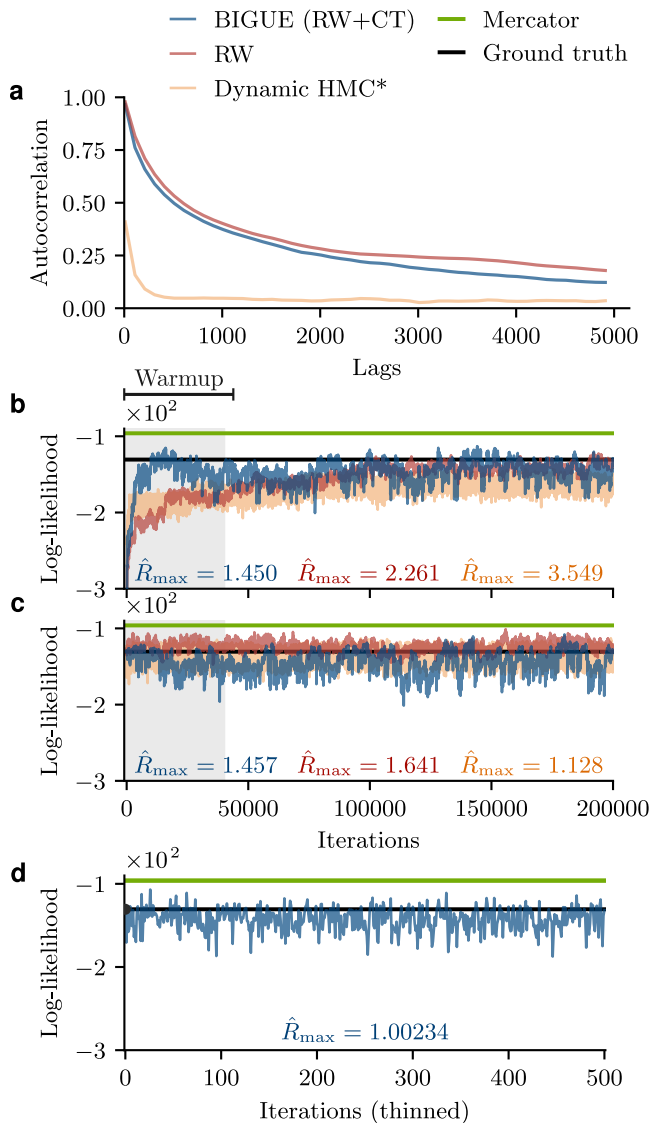


FIG. 3. Statistics of Markov chain Monte Carlo algorithms when embedding a synthetic graph in \mathbb{S}^1 . (a) Vertex and chain averaged autocorrelation for different lags. The autocorrelation of angular coordinates is adapted to consider their periodicity (see Appendix D). (b-c) Log-likelihood of a simulated Markov chain initialized with (panel b) and without (panel c) access to ground truth information. When ground truth is unknown, we initialize $\kappa_u = \deg(u)$ and draw the other parameters from their priors. (d) Log-likelihood of a Markov chain after thinning the chain shown in panel b. In each case, we compute \hat{R}_{\max} , the maximum potential scale reduction factor for all parameters after the warm-up (grey) — values close to 1 are desirable. The graph has 30 vertices and is generated with the \mathbb{S}^1 likelihood, with angular coordinates drawn from their prior, $\beta = 2.5$ and the κ parameters drawn from a Pareto distribution of parameter 2.5 and $\kappa_{\min} = 4$ and truncated to 10. Four independent chains were simulated to compute \hat{R} and the autocorrelation, but only one is displayed. The median effective sample sizes S_{eff} across all parameters were, for BIGUE: 500, 442, and 1608 (in panels b, c, and d respectively). For the random walk MCMC, we obtained medians of $S_{\text{eff}} = 236$, and 411, and for dynamic HMC, they were equal to 603 and 3837.

B. Cluster transformation MCMC

We can improve upon dynamic HMC and RW by noticing that the connection probability is a decreasing function of angular separation, such that groups of vertices at a large enough distance from one another are essentially independent. As a result, each region is akin to a smaller and simpler embedding problem, which is the basis for the approach of Wang et al. [41, 62]. (This is also the basis for the idea of renormalization in the \mathbb{H}^2 hyperbolic model in which groups of vertices are coarse-grained while partially preserving the structural integrity of the graph [1, 14].) Recalling that the likelihood is invariant to reflections and rotations, we propose to apply these transformations at the level of groups or clusters of vertices.

The first step for these new transformations is to partition vertices into roughly independent clusters given the angular positions. This is done by grouping vertices with an angular separation below some randomly sampled threshold in clusters. We use this naive partitioning scheme instead of an optimization procedure [65] for technical reasons discussed in Appendix C 2.

Once we have selected clusters, we apply one of the following transformations. The first transformation, named *flip*, applies a reflection on the vertices of the selected cluster. The second transformation, *exchange*, swaps the relative positions of two selected clusters. The third transformation, *translate*, moves the first selected cluster to the relative position of the second cluster. The first transformation explores local reflection symmetries, while the two others explore rotation symmetries. In each case we select the involved cluster(s) uniformly at random from all clusters.

Our proposed algorithm, BIGUE, combines these random cluster transformations (CT) with the random walk (RW) baseline. Cluster transformations explore the mesoscale structure of the embedding, while the random walk fine-tunes the embedding coordinates, including the parameters $\{\kappa_u\}$. Each sampling step is either a randomly selected CT or a short RW, and we calibrate the transition probabilities to the posterior distribution using the Metropolis-Hastings algorithm; see Appendix C for the technical details. (One could also combine random cluster transformations with HMC, but the high computational cost of HMC turns out to outweigh its benefits. A naive random walk provides cheaper and sufficient fine-tuning in our experiments.) We deal with the symmetries and automorphisms described in Sec. II B with a post-processing alignment step, in which we minimize the sum of angular separations to some arbitrary reference embedding over the automorphisms found by Nauty [66], the two possible reflections (reflection or no reflection) and the rotations $[0, 2\pi)$.

Figure 3 shows that BIGUE has a lower autocorrelation and reaches the typical set much faster than a pure RW algorithm. The fluctuations at equilibrium are also larger, which suggests that it explores the posterior more

efficiently. Furthermore, the maximum potential reduction factor \hat{R}_{\max} of BIGUE is lower than that of a random walk, suggesting that the algorithm has better mixing.

When comparing HMC to the complete Markov Chain generated with BIGUE, we note that autocorrelation decays far more slowly. Furthermore, BIGUE yields \hat{R} values above the recommended 1.01 threshold [67] (as do all the other algorithms). A direct fix is to *thin* the BIGUE chain, that is, only use every k -th sample point of the chain. Guided by Fig. 3a, we set $k = 10,000$ and obtain a $\hat{R}_{\max} < 1.01$ in, with the chain shown in Fig. 3c.

We note that Fig. 3 highlights one unintuitive aspect of continuous random variables: The neighborhood of the likelihood maximum accounts for a small fraction of the probability mass because probabilities are obtained through integration with respect to the Lebesgue measure. While the log-likelihood maximum (found by Mercator [33]) has a high probability density, its surroundings cover a larger volume (the typical set) and hold a much larger probability mass. Hence, our MCMC sample concentrates away from the maximum likelihood, as expected. (That said, we note that cluster transformations could easily be added to maximization routines if a point estimate was the goal, something we leave for future work.)

IV. UNCERTAIN EMBEDDINGS

A. Embedding and network properties

A proper quantification of the uncertainty inherent to the data is the primary reason for using a Bayesian method such as BIGUE. Figure 4 shows what such an analysis might look like, using credible intervals for the embedding coordinates and their transformations, computed with samples drawn from the chains depicted in Figure 3b.

The first to note is that BIGUE recovers the ground-truth coordinates, and so does Mercator. Posterior sampling reveals some leeway in the coordinates compatible with the data G , but they are firmly centered around the ground-truth values (Fig. 4a). As expected, for most vertices u , the κ_u parameters concentrate on the vertices' original degrees (Fig. 4b), but there are discrepancies. The relationship $\mathbb{E}[K(\kappa_u)] = \deg(u)$ is obtained by integrating the vertex density on the circle, which assumes an infinite number of vertices. This is why, for a high-degree vertex u in a small graph, κ_u is larger to compensate for the fact that there is a finite number of vertices. Figure 4c also shows that the posterior covers the original β value, although it is in a somewhat low probability region. The posterior distribution agrees with Mercator and places a higher likelihood than the ground truth on β being a bit under 2—this is due to random fluctuations in the instantiation of G conditioned on the ground truth coordinates.

Next, we turn to the properties of the graph. The edge

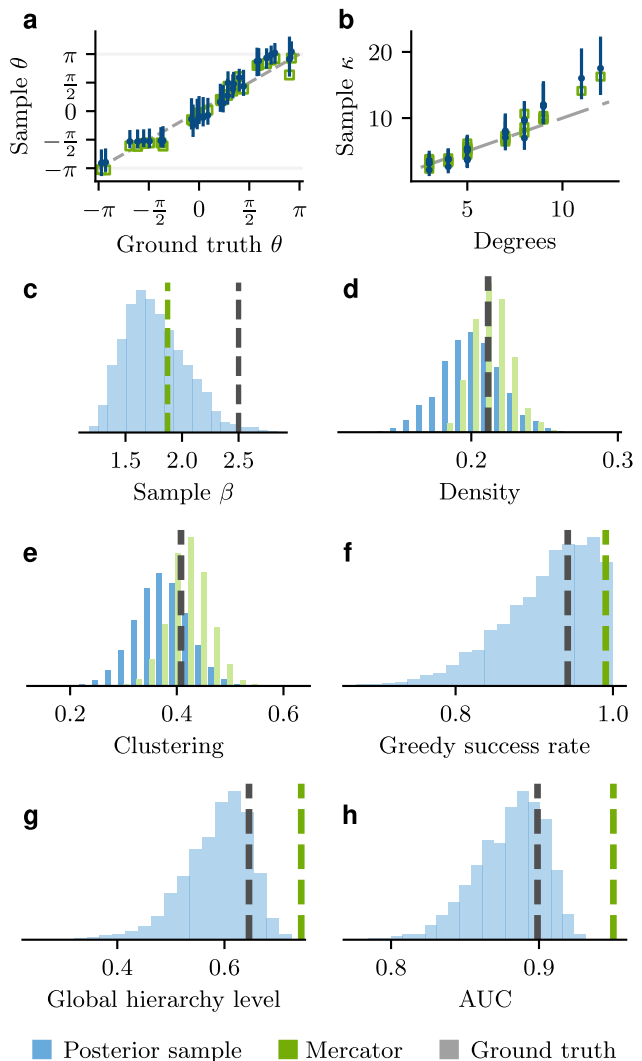


FIG. 4. Posterior estimates and posterior predictive distribution for the synthetic graph used in Fig. 3. (a) Angular coordinates $\{\theta_u\}$. (b) Parameters $\{\kappa_u\}$. (c) Inverse temperature β . (d) Density. (e) Clustering (the transitivity). (f) Greedy routing success rate. (g) Global hierarchy level [68]. (h) AUC of link prediction with embeddings coordinates and the \mathbb{S}^1 likelihood. In each case, 500 embeddings were sampled from four independent chains. In panels (c-h), the vertical dotted lines show point estimates computed with the Mercator and ground truth embeddings. In panels (a,b), points denote the median, and the error bars cover the first to third quartile. In panels (d,e), we generated graph samples for Mercator and the ground truth by conditioning the model's likelihood on point estimates of the embedding.

probabilities of good embeddings should yield graphs with properties similar to those of the original graph. As a result, if the embedding is accurate, we expect that the graphs generated with estimated coordinates will be similar to the original graph. We first verify this with Mercator, an optimization algorithm that provides a single embedding and, thus, a single random graph ensemble; the resulting distribution of graph properties is centered

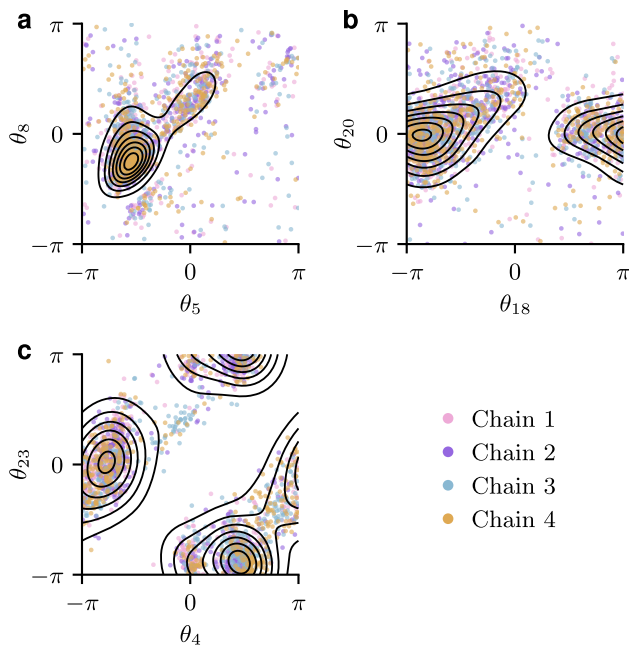


FIG. 5. Multimodality and non-normality of the posterior distribution, shown with the marginal posterior distributions of pairs of angular coordinates in the embedding of (a) the synthetic graph in Fig. 3 (b) Zachary’s karate club [69] (c) a synthetic graph containing a vertex whose position is drawn from a mixture. Each point is obtained with the thinned BIGUE algorithm, and chains comprise 500 random embeddings. The black lines delineate the density of a normal kernel density estimation of the marginal. To account for the periodicity, the kernel density is summed for rotations $\pm 2\pi$ in both axes.

around the observed graph in Fig. 4d,e. With BIGUE, each sample point corresponds to a random graph using the likelihood, and consequently, we can marginalize the graph properties over a much larger parameter space. (Formally, we can draw from the posterior predictive distribution of the model.) The resulting distributions are wider and now capture parameter uncertainty; see Fig. 4d,e again.

The embeddings also capture less obvious properties. For example, hyperbolic embeddings can play a role in finding effective and efficient greedy routing on the network. In the greedy routing algorithm, hyperbolic coordinates act as addresses, and one attempts to reach the target v from a source u by repeatedly following the edge that leads to the neighbor closest to the destination u (in hyperbolic space). The main issue with this algorithm is that paths can sometimes devolve into “greedy loops” that lead nowhere. The *greedy success rate* evaluates the extent to which this is an issue as the proportion of greedy routes that successfully reach their destination. Our posterior samples allow us to compute error bars for this property of the graph *and* embedding, as shown in Fig. 4f. In this particular synthetic graph, many plausible embeddings lead to a greedy routing comparable to

Mercator, but the majority is less reliable.

The hierarchy of graphs is another example of complex properties captured by hyperbolic embeddings. Garcia et al. [68] introduced the *global hierarchy level* to quantify this, using a function of the angular distance between neighboring nodes with coordinates in the outer and inner parts of the embedding. Figure 4g illustrates how, for the synthetic graph analyzed, most plausible embeddings have smaller global hierarchy levels than both the ground truth and the Mercator embedding.

Finally, embeddings for the \mathbb{S}^1 model can be viewed as classifiers for edges since the likelihood maps potential edges (binary classes) to edge probabilities. If the embedding is a good representation of the graph, edges should have a high probability, while non-edges should have a low probability. As a simple test of link prediction, we used the embedding positions and the likelihood (2) to assign probabilities to pairs of nodes. We then quantified the quality of this classifier with the area under the receiver operating characteristic curve (AUC), with a score of 1 indicating perfect edge prediction. Figure 4h reveals that Mercator’s embedding yields the best classifier, while BIGUE’s embeddings are as useful as the ground-truth coordinates. This suggests that BIGUE reports more typical embeddings of the model while Mercator overfits the coordinates to reproduce exactly the same graph.

B. Multimodality

Next, we inspect the properties of the posterior distribution of coordinates in more detail. MCMC algorithms are computationally expensive, and one might wonder if we could do away with sampling altogether—be it HMC, BIGUE, or another algorithm—by quantifying uncertainty with Laplace’s approximation or a variational approach [75] instead. These approximations are attractive because they yield error bars for all quantities nearly for free, and they have strong theoretical backing, e.g., the Bernstein–von Mises theorem that guarantees convergence to the approximated distribution in the big data regime under certain conditions. Unfortunately, for small graphs and \mathbb{S}^1 , at the very least, we find that they are not appropriate and that MCMC is truly necessary.

Treating our sample as truly representative of the posterior distribution, we computed the p-values of the Henze-Zirkler normality test for all pairs of parameters and found the largest to be 4.82×10^{-14} for the example synthetic graph. This is not surprising when looking at the marginal distribution of the pair of coordinates shown in Fig. 5a: the bulk of the distribution is skewed, and there is a region of very low probability mass next to the bulk. All marginalizations of a multivariate normal yield another multivariate normal; thus, finding one non-normal marginal is enough to reject it as a model for the whole.

It could be that only synthetic graphs show non-normal

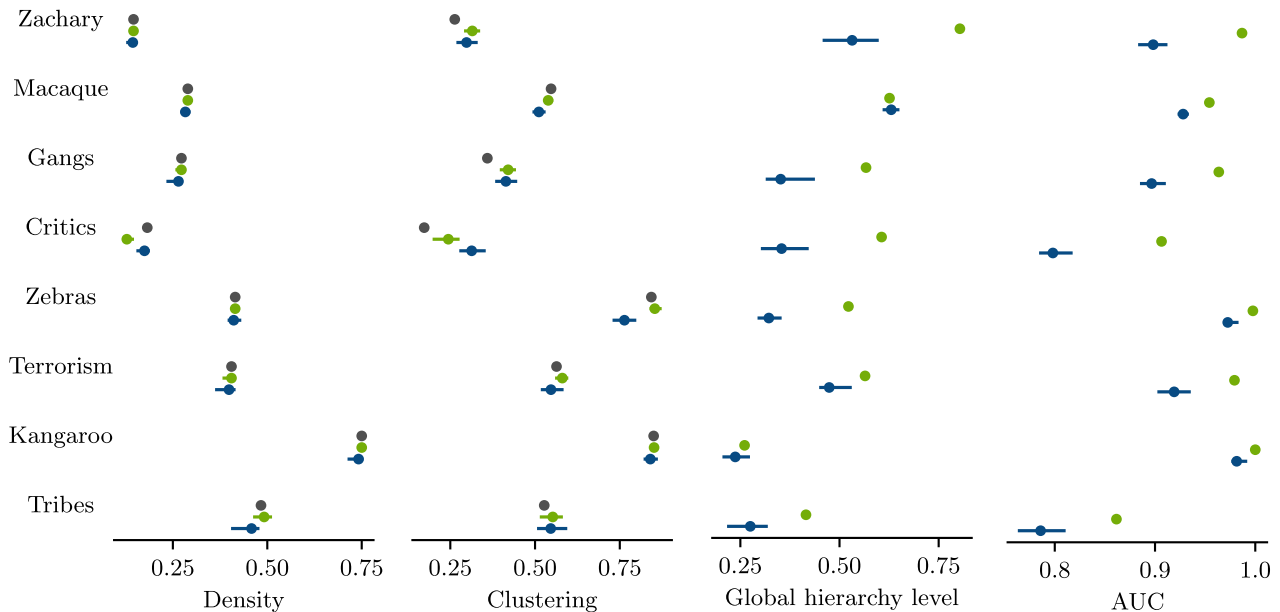


FIG. 6. Comparison of network embeddings obtained from a maximum likelihood estimator (Mercator) and the posterior of a Bayesian model (BIGUE) for various empirical networks: Zachary’s karate club [69], cortical connectivity of the macaque [70], street gangs in Montreal [71], dutch literary critics [72], zebra social interactions [73], connections in greek terrorist group [74], kangaroo dominance relationships [74] and New Guinea tribes friendships. Vertices outside the largest connected components were removed in order to run Mercator. The horizontal bars show 50% highest density intervals, and points within are the median. Table I reports the values for this figure.

posterior distributions, but it turns out that the embedding of well-known graphs not explicitly generated by the model behaves the same way. For example, the posterior of Zachary’s Karate Club is also not normal, with a maximal p-value of 10^{-4} for the Henze-Zirkler normality test; Fig. 5b shows that joint marginals for this graph are not ellipsoids.

One of the most compelling pieces of evidence for the non-normality of hyperbolic embeddings, is the ease with which it can be induced using a mixture for the embedding coordinates. A simple procedure that achieves multimodality is as follows. First, we give random coordinates to the vertices as usual. But when we generate the edges of G , we use either the original or an updated angular coordinate for a single vertex u (e.g., $\theta_u \mapsto \theta_u + 2 \bmod 2\pi$), with probability 0.5, thereby connecting u to two incompatible sets of vertices. Figure 5c shows the marginal distribution of two angular positions for the resulting graph. Neither of these two chosen vertices is the vertex with a superposition of angular coordinates, yet the marginal is clearly multimodal. In our experiments, we also found that almost all joint marginals that include at least one angular coordinate are bimodal; a single vertex with an ambiguous position is sufficient to induce the behavior.

C. Observational study

To conclude our analysis, we embed a collection of empirical networks with BIGUE and contrast our results with Mercator’s; the experiments are summarized in Fig. 6 (see Appendix for a table giving numerical values in a table). Both algorithms reproduce the observed density and clustering (transitivity) of the graph. However, as we have argued above, Mercator yields a single embedding and thus ignores parameter uncertainty, leading to tighter estimated intervals.

Properties that only depend on coordinates, like the global hierarchy level, have no associated ground truth in observational data and can only be compared across different embedding algorithms. Except for the macaque neural network, we find that Mercator systematically yields higher values of the hierarchy than BIGUE’s, usually by a large margin. This suggests that graphs are less hierarchical than they might seem if we only used Mercator embedding as the source of truth.

Finally, the link prediction results clearly show that finding a good representation for data is somewhat of an orthogonal goal to optimizing for prediction performance [76]. These results suggest that Mercator overfits to the observed graph to provide a better prediction of the links, while the posterior estimate selects the most plausible model while discounting statistical fluctuations.

V. CONCLUSION

Hyperbolic random graphs are unquestionably useful and can explain many properties observed in empirical networks, but existing estimation algorithms neglect the significant uncertainty and multimodality that can be present in these models, while off-the-shelf uncertainty quantification methods fall short. We provided evidence that the state-of-the-art dynamic HMC is unable to sample the posterior of a Bayesian hyperbolic embedding model and that supplementing random cluster transformations to a generic random walk is sufficient to sample embeddings of small graphs. Maximum likelihood estimators provided by Mercator overfit the coordinates do not provide error bars on embedding. This motivated us to introduce BIGUE, an MCMC algorithm with cluster transformations that provide an accurate posterior sample for the error bars on the graph and embedding properties.

As future work, we believe that generalizing cluster transformation on the $D + 1$ -sphere could be promising for developing effective sampling algorithms for the \mathbb{H}^D hyperbolic model [49]. It's very likely that HMC can be tweaked to perform better since there is a finite number of discontinuities, and this should also help a generalization in higher dimensions. Finally, the effectiveness of cluster transformations for sampling suggests that they could also be used to improve existing likelihood maximization algorithms.

ACKNOWLEDGMENTS

This work was supported by Conseil de recherches en sciences naturelles et en génie du Canada (AA), Sentinelle Nord (SL, AA) and the Fonds de recherche du Québec (SL). We acknowledge Calcul Québec and Alliance de recherche numérique du Canada for their technical support and computing infrastructures.

SOFTWARE

A Python implementation of BIGUE is available on GitHub at <https://github.com/DynamicaLab/bigue>.

REFERENCES

- [1] M. Boguñá, I. Bonamassa, M. De Domenico, S. Havlin, D. Krioukov, and M. Á. Serrano, *Nat. Rev. Phys.* **3**, 114 (2021).
- [2] T. Munzner, *IEEE Comput. Graph. Appl.* **18**, 18 (1998).
- [3] B. Kovács and G. Palla, *Sci. Rep.* **11**, 16050 (2021).
- [4] D. V. Foster, J. G. Foster, P. Grassberger, and M. Paczuski, *Phys. Rev. E* **84**, 066117 (2011).
- [5] S. G. Balogh, B. Kovács, and G. Palla, *Commun. Phys.* **6**, 1 (2023).
- [6] S. G. Balogh and G. Palla, *Intra-Community Link Formation and Modularity in Ultracold Growing Hyperbolic Networks*, Preprint arXiv:2401.17983 (2024).
- [7] K. Zuev, M. Boguñá, G. Bianconi, and D. Krioukov, *Sci. Rep.* **5**, 9421 (2015).
- [8] D. Krioukov, F. Papadopoulos, M. Kitsak, A. Vahdat, and M. Boguñá, *Phys. Rev. E* **82**, 036106 (2010).
- [9] L. Gugelmann, K. Panagiotou, and U. Peter, in *Automata, Languages, and Programming* (2012) pp. 573–585.
- [10] D. Krioukov, *Phys. Rev. Lett.* **116**, 208302 (2016).
- [11] E. Candellero and N. Fountoulakis, in *Algorithms and Models for the Web Graph* (2014) pp. 1–12.
- [12] M. Boguñá, D. Krioukov, P. Almagro, and M. Á. Serrano, *Phys. Rev. Research* **2**, 023040 (2020).
- [13] M. Zheng, A. Allard, P. Hagmann, Y. Alemán-Gómez, and M. Á. Serrano, *Proc. Natl. Acad. Sci. U.S.A.* **117**, 20244 (2020).
- [14] G. García-Pérez, M. Boguñá, and M. Á. Serrano, *Nat. Phys.* **14**, 583 (2018).
- [15] C. Song, S. Havlin, and H. A. Makse, *Nature* **433**, 392 (2005).
- [16] M. Boguñá, D. Krioukov, and K. C. Claffy, *Nat. Phys.* **5**, 74 (2009).
- [17] M. Boguñá, F. Papadopoulos, and D. Krioukov, *Nat. Commun.* **1**, 62 (2010).
- [18] F. Papadopoulos, D. Krioukov, M. Boguna, and A. Vahdat, in *2010 Proceedings IEEE INFOCOM* (2010) pp. 1–9.
- [19] A. Baptista, R. J. Sánchez-García, A. Baudot, and G. Bianconi, *Zoo Guide to Network Embedding*, Preprint arXiv:2305.03474 (2023).
- [20] H. Cai, V. W. Zheng, and K. C.-C. Chang, *IEEE Trans. Knowl. Data Eng.* **30**, 1616 (2018).
- [21] Y.-J. Zhang, K.-C. Yang, and F. Radicchi, *Phys. Rev. E* **104**, 044315 (2021).
- [22] D. McDonald, *The Hierarchical Organisation and Dynamics of Complex Networks*, Ph.D. thesis, University of Birmingham (2021).
- [23] P. Goyal and E. Ferrara, *Knowl.-Based Syst.* **151**, 78 (2018).
- [24] K. Chowdhary and T. G. Kolda, *J. Complex Netw.* **6**, 321 (2018).
- [25] M. Keller-Ressel and S. Nargang, *J. Complex Netw.* **8**, cnaa002 (2020).
- [26] F. Sala, C. D. Sa, A. Gu, and C. Re, in *Proceedings of the 35th International Conference on Machine Learning* (2018) pp. 4460–4469.
- [27] K. Verbeek and S. Suri, *Comput. Geom.* **59**, 1 (2016).
- [28] J. R. Clough and T. S. Evans, *PLOS ONE* **12**, e0187301 (2017).
- [29] R. Sarkar, in *Graph Drawing* (2012) pp. 355–366.
- [30] B. P. Chamberlain, J. Clough, and M. P. Deisenroth, *Neural Embeddings of Graphs in Hyperbolic Space*, Preprint arXiv:1705.10359 (2017).
- [31] C. V. Cannistraci, G. Alanis-Lobato, and T. Ravasi, *Bioinformatics* **29**, i199 (2013).
- [32] A. Muscoloni, J. M. Thomas, S. Ciucci, G. Bianconi, and C. V. Cannistraci, *Nat. Commun.* **8**, 1615 (2017).
- [33] G. García-Pérez, A. Allard, M. Á. Serrano, and M. Boguñá, *New J. Phys.* **21**, 123033 (2019).
- [34] F. Papadopoulos, C. Psomas, and D. Krioukov, *IEEE/ACM Trans. Netw.* **23**, 198 (2015).

- [35] F. Papadopoulos, R. Aldecoa, and D. Krioukov, *Phys. Rev. E* **92**, 022807 (2015).
- [36] G. Alanis-Lobato, P. Mier, and M. A. Andrade-Navarro, *Appl. Netw. Sci.* **1**, 1 (2016).
- [37] G. Alanis-Lobato, P. Mier, and M. A. Andrade-Navarro, *Sci. Rep.* **6**, 30108 (2016).
- [38] Z. Wang, Q. Li, W. Xiong, F. Jin, and Y. Wu, *Physica A* **452**, 178 (2016).
- [39] Z. Wang, Y. Wu, Q. Li, F. Jin, and W. Xiong, *Physica A* **450**, 609 (2016).
- [40] T. Bläsius, T. Friedrich, A. Krohmer, and S. Laue, *IEEE/ACM Trans. Netw.* **26**, 920 (2018).
- [41] Z. Wang, L. Sun, M. Cai, and P. Xie, *J. Stat. Mech.* **2019**, 123401 (2019).
- [42] D. Ye, H. Jiang, Y. Jiang, Q. Wang, and Y. Hu, *Knowl.-Based Syst.* **246**, 108699 (2022).
- [43] Z. Wu, Z. Di, and Y. Fan, *Complexity* **2020**, e8372928 (2020).
- [44] B. Kovács and G. Palla, *Commun. Phys.* **6**, 1 (2023).
- [45] A. Allard, M. Á. Serrano, and M. Boguñá, *Nat. Phys.* **20**, 150 (2024).
- [46] S. Yi, H. Jiang, Y. Jiang, P. Zhou, and Q. Wang, *IEEE Trans. Netw. Sci. Eng.* **8**, 599 (2021).
- [47] A. Allard, M. Á. Serrano, G. García-Pérez, and M. Boguñá, *Nat. Commun.* **8**, 14103 (2017).
- [48] R. Jankowski, P. Hozhabrierdi, M. Boguñá, and M. Á. Serrano, *Feature-Aware Ultra-Low Dimensional Reduction of Real Networks*, Preprint arXiv:2401.09368 (2024).
- [49] R. Jankowski, A. Allard, M. Boguñá, and M. Á. Serrano, *Nat. Commun.* **14**, 7585 (2023).
- [50] M. Kitsak, I. Voitalov, and D. Krioukov, *Phys. Rev. Research* **2**, 043113 (2020).
- [51] M. Papamichalis, K. Turnbull, S. Lunagomez, and E. Airoldi, *Latent Space Network Modelling with Hyperbolic and Spherical Geometries*, Preprint arXiv:2109.03343 (2022).
- [52] Y. Yao, A. Vehtari, and A. Gelman, *J. Mach. Learn. Res.* **23**, 1 (2022).
- [53] Y. Yao, C. Cademartori, A. Vehtari, and A. Gelman, *Adaptive Path Sampling in Metastable Posterior Distributions*, Preprint arXiv:2009.00471 (2020).
- [54] G. West, Z. Sinkala, and J. Wallin, *Front. Appl. Math. Stat.* **8**, 915294 (2022).
- [55] H. Tjelmeland and B. K. Hegstad, *Scand. J. Stat.* **28**, 205 (2001).
- [56] E. Pompe, C. Holmes, and K. Łatuszyński, *Ann. Stat.* **48**, 2930 (2020).
- [57] J. Park, *Sampling from Multimodal Distributions Using Tempered Hamiltonian Transitions*, Preprint arXiv:2111.06871 (2021).
- [58] R. M. Neal, *Stat. Comput.* **6**, 353 (1996).
- [59] S. Lan, J. Streets, and B. Shahbaba, *Proc. Innov. Appl. Artif. Intell. Conf.* **2014**, 1953 (2014).
- [60] M. M. Graham and A. J. Storkey, *Continuously Tempered Hamiltonian Monte Carlo*, Preprint arXiv:1704.03338 (2017).
- [61] A. Faqeeh, S. Osat, and F. Radicchi, *Phys. Rev. Lett.* **121**, 098301 (2018).
- [62] Z. Wang, Q. Li, F. Jin, W. Xiong, and Y. Wu, *Physica A* **455**, 104 (2016).
- [63] M. Betancourt, *A Conceptual Introduction to Hamiltonian Monte Carlo*, Preprint arXiv:1701.02434 (2018).
- [64] B. Carpenter, A. Gelman, M. D. Hoffman, D. Lee, B. Goodrich, M. Betancourt, M. Brubaker, J. Guo, P. Li, and A. Riddell, *J. Stat. Softw.* **76**, 1 (2017).
- [65] A. Patania, A. Allard, and J.-G. Young, *Proc. R. Soc. A* **479**, 20230159 (2023).
- [66] B. D. McKay and A. Piperno, *J. Symb. Comput.* **60**, 94 (2014).
- [67] A. Vehtari, A. Gelman, D. Simpson, B. Carpenter, and P.-C. Bürkner, *Bayesian Anal.* **16**, 667 (2021).
- [68] G. García-Pérez, M. Boguñá, A. Allard, and M. Á. Serrano, *Sci. Rep.* **6**, 33441 (2016).
- [69] W. W. Zachary, *J. Anthropol. Res.* **33**, 452 (1977), 3629752.
- [70] M. P. Young, *Proc. R. Soc. B* **252**, 13 (1997).
- [71] K. Descormiers and C. Morselli, *Int. Crim. Justice Rev.* **21**, 297 (2011).
- [72] W. de Nooy, *Poetics* **26**, 385 (1999).
- [73] S. R. Sundaresan, I. R. Fischhoff, J. Dushoff, and D. I. Rubenstein, *Oecologia* **151**, 140 (2007).
- [74] C. J. Rhodes and P. Jones, *J. Oper. Res. Soc.* **60**, 1373 (2009).
- [75] D. M. Blei, A. Kucukelbir, and J. D. McAuliffe, *J. Am. Stat. Assoc.* **112**, 859 (2017).
- [76] T. Vallès-Català, T. P. Peixoto, M. Sales-Pardo, and R. Guimerà, *Phys. Rev. E* **97**, 062316 (2018).
- [77] A. Gelman and D. B. Rubin, *Stat. Sci.* **7**, 457 (1992).
- [78] A. Gelman, J. B. Carlin, H. S. Stern, D. B. Dunson, A. Vehtari, and D. B. Rubin, *Bayesian Data Analysis*, 3rd ed. (CRC Press, 2013).
- [79] A. Sokal, in *Functional Integration*, edited by C. DeWitt-Morette, P. Cartier, and A. Folacci (Springer US, 1997) pp. 131–192.
- [80] S. R. Jammalamadaka and A. Sengupta, *Topics In Circular Statistics* (World Scientific Publishing, 2001).

Appendix A: Relationship between \mathbb{S}^1 and \mathbb{H}^2

While we developed our algorithm for the \mathbb{S}^1 formulation of hyperbolic random graphs, some measures, like the greedy success rate, and visualization such as Fig. 1 require the hyperbolic coordinates in \mathbb{H}^2 embedding. They are formally related by coordinate transformation

$$r_u = R_{\mathbb{H}} - 2 \ln \frac{\kappa_u}{\kappa_{\min}} \quad (\text{A1})$$

with $R_{\mathbb{H}} = 2 \ln \frac{|V|}{\mu\pi\kappa_{\min}}$ where $\kappa_{\min} > 0$ is the smallest allowable κ value (we set $\kappa_{\min} = 1$), edge probabilities in the \mathbb{S}^1 model can be rewritten as

$$\mathbb{P}[(u, v) \in E \mid x, \beta] = \frac{1}{1 + \exp\left(\beta(r_u + r_v + 2 \ln \frac{\Delta(\theta_u, \theta_v)}{2}) - R_{\mathbb{H}}\right)}. \quad (\text{A2})$$

We retrieve the HRGM connection probability

$$\mathbb{P}[(u, v) \in E \mid x, \beta] = \frac{1}{1 + \exp(\beta(d_{\mathbb{H}}(x_u, x_v) - R_{\mathbb{H}}))} \quad (\text{A3})$$

using the following approximation of the hyperbolic distance

$$\begin{aligned} d_{\mathbb{H}}(x_u, x_v) &= \operatorname{arccosh} \left(\cosh(r_u) \cosh(r_v) \right. \\ &\quad \left. - \sinh(r_u) \sinh(r_v) \cos(\theta_u - \theta_v) \right), \\ &\approx r_u + r_v + 2 \ln \frac{\Delta(\theta_u, \theta_v)}{2}, \end{aligned} \quad (\text{A4})$$

where $x_u = (r_u, \theta_u)$ is the position of vertex u , and r_u and θ_u are, respectively, the radial and angular coordinates in the hyperboloid model.

Appendix B: Continuous \mathbb{S}^1 model

As shown in Fig. 2, the gradient of the likelihood is undefined when two vertices u and v have the same angular coordinate $\theta_u = \theta_v$. The culprit is the derivative of $\Delta(\theta_u, \theta_v)$ with respect to θ_u , since the function contains two absolute values. For a given value of θ_v , we have that $-\pi + \theta_v \leq \theta_u < \pi + \theta_v$, which contains at most three discontinuities: $\theta_u = \theta_v$ and $\theta_u - \theta_v \in \{-2\pi, -\pi, \pi, 2\pi\}$. One way to smoothen these sharp transitions is to replace each absolute value with

$$|x| \approx x \left(\frac{2}{1 + e^{-bx}} - 1 \right) := \tilde{a}(x). \quad (\text{B1})$$

This approximation is exact in the limit of $b \rightarrow \infty$, which allows us to control the sharpness of the gradient changes. Beyond the obvious distortions around the discontinuities, another artifact this approximation causes

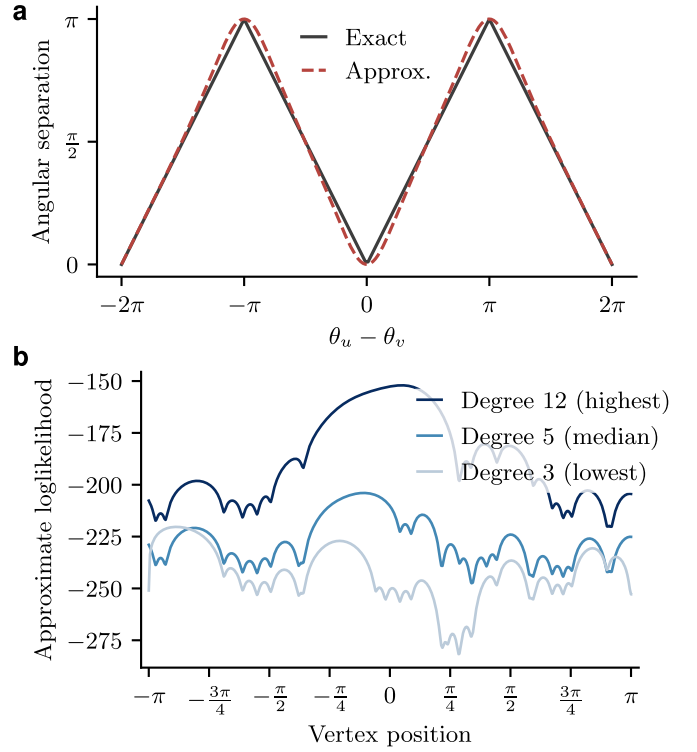


FIG. 7. (a) Continuous approximation of the angular separation with $b = 3$. (b) Figure 2 using the continuous \mathbb{S}^1 model approximation with $b = 3$. The approximate angular separation is not invariant to rotations because the gradient doesn't decrease to 0 at $\theta_u = \theta_v$ and at $\theta_u - \theta_v = \pm\pi$. The gradient discontinuities are gone at the cost of distortions of the likelihood.

is the loss of rotation symmetry: the gradient doesn't decrease to 0 at $\pm 2\pi$, while it does at $\theta_u = \theta_v$ and $\theta_u - \theta_v = \pm\pi$, where the approximation is used. Further, while $\tilde{a}(0) = 0$, the approximate separation is not zero for $\theta_u = \theta_v$, because $\pi - \tilde{a}(\pi) > 0$.

We found in practice that using $b > 3$ caused gradient divergences in Stan. Figure 7 compares the exact angular separation to the approximate one with $b = 3$. While the error seems small, densely connected groups of vertices are usually tightly grouped in hyperbolic space, which can result in incorrect embeddings.

Appendix C: Metropolis-Hastings sampling

The Metropolis-Hastings algorithm generates Markov chains with arbitrary target invariant measures by (i) sampling transitions between states from a proposal distribution and (ii) accepting or rejecting new states with a carefully crafted acceptance probability. More specifically, the acceptance probability of new state x^* given

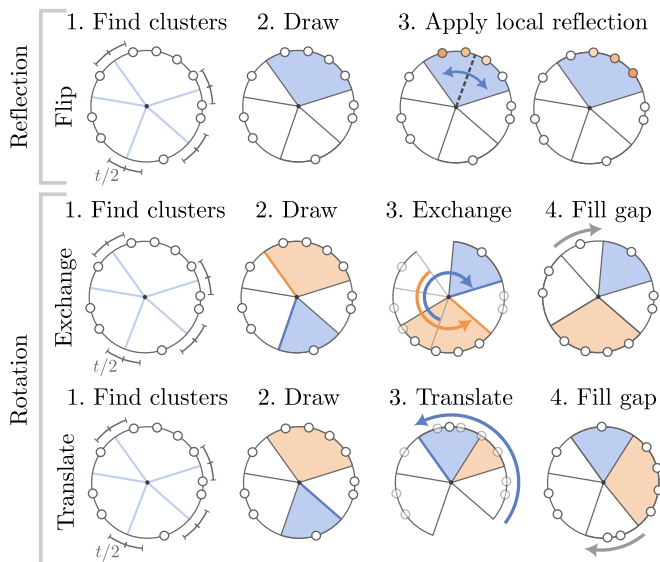


FIG. 8. Summary of the cluster transformations used in BIGUE. The “flip” transformation targets the reflection symmetries, and the “exchange” and “translate” transformations target the rotation symmetries.

the previous state x for a continuous random variable is

$$\alpha(x^*, x) = \frac{p(x^*)q(x|x^*)}{p(x)q(x^*|x)}, \quad (\text{C1})$$

where $q(x^*|x)$ is the density of the transition kernel, that is, the density of sampling new state x^* from state x . In this Appendix, the target p is always the posterior distribution of the Bayesian model.

As explained in the text, we define a global transition kernel, which selects sub-kernels randomly, proportional to their weight: 0.4 for a random walk and 0.2 for each cluster transformation defined in the main text and illustrated in Fig. 8. We will design all sub-kernels with the target p as their stationary measures, meaning that the proposed state of a subkernel can be accepted with probability 1. The weights are canceled in the acceptance probability and their sole purpose is to help the chain mixing.

1. Random walk

For the Markov chain to be irreducible, the sampling space must be accessible from every neighborhood. This is easily satisfied using a random walk algorithm. In this algorithm, a new state x^* is sampled using a normal distribution centered around the previous state x . When the random walk subkernel is selected by the global kernel, the set of parameters to explore—that is $\{\theta_u\}$, $\{\kappa_u\}$ or $\{\beta\}$ —is chosen randomly with equal probability. The main challenge of a random walk Metropolis-Hastings is tuning the variance of the kernel. This becomes increasingly difficult in high dimensions: a large variance leads

to most proposals being rejected, and a small variance leaves the chain in the same region, increasing the auto-correlation and the mixing time in both cases. Hence, we focus on local perturbations.

For uniformly distributed vertices on the circle, the distribution of angular separation between two geometrically adjacent vertices is approximately (because of the periodicity on the circle) the exponential distribution of parameter $2\pi/|V|$. To preserve the angular order of vertices on average, we sample each θ_u from

$$\Theta_u^* = \theta_u + \varepsilon \pmod{2\pi}, \quad \varepsilon \sim \mathcal{N}_{[-\pi, \pi]}(0, (\pi/2|V|)^2), \quad (\text{C2})$$

where $\mathcal{N}_{[-\pi, \pi]}$ is the truncated normal distribution on the interval $[-\pi, \pi]$ and where $x \pmod{2\pi}$ adjusts x such that it lies in $[-\pi, \pi]$. Since the normal distribution is symmetric, there is no bias induced from this transformation $q(\theta^*|\theta) = q(\theta|\theta^*)$.

The transition kernel for κ and β is a lower truncated normal kernel

$$x^* \sim \mathcal{N}_{(x_{\min}, \infty)}(x, \sigma_x^2), \quad (\text{C3})$$

where x_{\min} is the smallest value for the parameter x . When applying the random walk onto $\{\kappa_u\}$, each κ_u^* is independently sampled from Eq. (C3). The normalization for Eq. (C3) cannot be omitted when computing the ratio of q in Eq. (C1) because it depends on x . We use $\sigma_\kappa = 0.5$ since κ 's order of magnitude is the degree and $\sigma_\beta = 0.3$ is quite small because β has a global impact on the connection probabilities. We use $\kappa_{\min} = \epsilon$, $\beta_{\min} = 1$ for consistency with the priors.

2. Cluster transformations

For given angular positions θ , we partition the vertices into clusters \mathcal{C} such that every pair of geometric neighbors θ_i and θ_j in the same cluster has an angular separation $\Delta(\theta_i, \theta_j)$ below a threshold t . The two geometric neighbors of a vertex are the closest vertices in the clockwise and counter-clockwise direction of the circle. The partition of the vertex set is converted to a partition of the circle by defining the boundaries of clusters as the midpoints between each cluster's endpoints.

Because the cluster transformations are discrete, we define subkernel's probability *mass* function $Q[\Theta^* = \theta^*|\theta]$, which gives the probability of sampling a new set of positions θ^* when the coordinates are currently equal to θ . For the cluster transformation, the acceptance probability is thus

$$\alpha(\theta^*, \theta) = \frac{p(\theta^*|G)Q[\Theta^* = \theta|\theta^*]}{p(\theta|G)Q[\Theta^* = \theta^*|\theta]}, \quad (\text{C4})$$

Each cluster transformation operates on a subset of the partition $\Lambda \subseteq \mathcal{C}$ containing a predetermined number of clusters. For instance, when we apply a translation

and move cluster C_1 to the position of cluster C_2 , then $\Lambda = \{C_1, C_2\}$ and \mathcal{C} is any partition such that $\mathcal{C} \supseteq \Lambda$. Since Λ is not ordered, we choose to translate C_1 to C_2 or C_2 to C_1 with equal probability: $\mathbb{P}[\Theta^* = \theta^* | \Lambda, \theta] = 1/2$. (This detail does not arise for the flip transformation because it involves a single cluster, and likewise for the swap transformation because it is symmetric.)

The probability Q of sampling the new state is found by marginalizing over all admissible partitions \mathcal{C} (i.e., supersets of Λ)

$$Q[\Theta^* = \theta^* | \theta] = \sum_{\mathcal{C} \supseteq \Lambda} \mathbb{P}[\Theta^* = \theta^* | \Lambda, \theta] \mathbb{P}[\Lambda = \Lambda | \theta], \quad (\text{C5})$$

where $\mathbb{P}[\Lambda = \Lambda | \theta]$ is the probability of proposing clusters Λ . This equation holds if the cluster transformation only yields θ^* when operating on that specific Λ . This is the case for our cluster transformations except for very specific θ that have measure zero.

To define and calculate $\mathbb{P}[\Lambda = \Lambda | \theta]$, we first note that a partition \mathcal{C} usually contains more clusters than what is strictly required by the transformation, and so we choose Λ randomly from \mathcal{C} . When there isn't a sufficient number of clusters in the sampled partition \mathcal{C} , the proposed θ^* is automatically rejected. For the sake of simplicity and efficiency, we use a uniform distribution corresponding to

$$\mathbb{P}[\Lambda = \Lambda | \mathcal{C}, \theta] = \left(\frac{|\mathcal{C}|}{|\Lambda|} \right)^{-1}. \quad (\text{C6})$$

(Targeted cluster selection could be an interesting future research direction.)

Since the hyperbolic space has a hierarchical structure, natural clusters can emerge at different scales, and we found it helpful to use a random threshold T to sample the partitions. This adds a bit of mathematical complexity, as we will now need to think of the cluster proposal probability $\mathbb{P}[\Lambda = \Lambda | \theta]$ as the marginal of $\mathbb{P}[\Lambda = \Lambda, \mathcal{C} | \theta]$ over all partitions. To compute this probability, we note that there exists an interval of threshold values $T \in [t, t']$ that yields the same partition \mathcal{C} . Since our partitioning algorithm is otherwise deterministic, we can convert the probability of sampling a particular partition \mathcal{C} to the probability of sampling the threshold in that interval,

$$\mathbb{P}[\mathcal{C} = \mathcal{C} | \theta] = \mathbb{P}[T \in [t, t'] | \theta], \quad (\text{C7})$$

where \mathcal{C} is the random variable of the partition. A uniform distribution over $[0, \pi]$ might seem reasonable for T , but it turns out to be a poor choice because the density of vertices per radian depends on the graph's size. In other words, for the same threshold value, increasing the number of vertices would eventually lead us to propose a single cluster with probability close to 1 (unless there are gaps that never contain any vertices).

To take this into consideration, we parameterize the distribution of T using the probability ξ that at least one vertex u is within the separation threshold t of another

vertex v

$$\xi := \mathbb{P}[\exists u : |\theta_u| < t/2] = 1 - \left(1 - \frac{t}{\pi}\right)^{|V|-1}, \quad (\text{C8})$$

where we assume that the angles are uniformly distributed and set $\theta_v = 0$ without loss of generality. By rearranging this equation, we get

$$t(|V|, \xi) = \pi(1 - (1 - \xi)^{1/(|V|-1)}). \quad (\text{C9})$$

In the algorithm, we draw T , by analogy to the random walk subkernel for the embedding coordinates:

$$T \sim \mathcal{N}_{[0, \pi]}(t(|V|, 0.9), (\pi/2|V|)^2). \quad (\text{C10})$$

In order to compute Eq. (C5), we need an efficient way to find every partition $\mathcal{C} \supseteq \Lambda$ and another to find the intervals $[t, t']$ of Eq. (C7). Luckily, our partitioning algorithm makes this feasible: A cluster can only shrink as T decreases and can only grow as T increases. This means that given Λ and θ , all valid partitions $\mathcal{C} \subseteq \Lambda$ are obtained within an interval $T \in [t_{\min}, t_{\max}]$. The values of $t_{\min}(\Lambda)$ and $t_{\max}(\Lambda)$ are the largest in-cluster and the smallest inter-cluster angular separations found for any cluster of Λ respectively

$$t_{\min}(\Lambda) = \max_{C_j \in \Lambda} \max_{\substack{u \in C_j \\ v \in \mathcal{A}(u) \cap C_j}} \Delta(\theta_u, \theta_v), \quad (\text{C11})$$

$$t_{\max}(\Lambda) = \min_{C_j \in \Lambda} \min_{\substack{u \in C_j \\ v \in \mathcal{A}(u) \setminus C_j}} \Delta(\theta_u, \theta_v), \quad (\text{C12})$$

where $\mathcal{A}(u)$ is the set of geometric neighbors of u . The inner maximum of Eq. (C11) is set to 0 when C_j contains only u and the inner minimum of Eq. (C12) is set to π when C_j contains all the vertices (they are ill-defined otherwise).

We now determine the thresholds within (t_{\min}, t_{\max}) for which the partition changes, which, here, is when the number of clusters changes. These intermediary thresholds are in fact the angular separations of geometrically adjacent vertices outside the required clusters (noted $\{u \notin \Lambda\}$)

$$\{\Delta(\theta_u, \theta_v) | u \notin \Lambda, v \in \mathcal{A}(u)\} \cap (t_{\min}, t_{\max}). \quad (\text{C13})$$

These are used to partition the admissible thresholds

$$[t_{\min}, t_{\max}] = [t_{\min}, t_1] \cup [t_1, t_2] \cup \dots \cup [t_k, t_{\max}], \quad (\text{C14})$$

where k is the number of intermediary thresholds and t_i is the i th intermediary threshold in ascending order. Hence, denoting $I(\Lambda)$ the set of these subintervals,

$$\mathbb{P}[\Lambda = \Lambda | \theta] = \sum_{[t, t'] \in I(\Lambda)} \mathbb{P}[\Lambda = \Lambda | \mathcal{C}, \theta] \mathbb{P}[T \in [t, t'] | \theta], \quad (\text{C15})$$

where, with a slight abuse of notation, we have used the fact \mathcal{C} is the partition obtained for thresholds $T \in [t, t']$.

We note that Eq. (C4) is derived from a detailed balance, and thus requires that $Q[\Theta^* = \theta|\theta^*] > 0$ if and only if $Q[\Theta^* = \theta|\theta] > 0$, meaning that each transformation should be reversed by a single Markov transition. This is always the case for our cluster-based transformations because each one can be undone when they operate on the same Λ . Our partitioning technique also ensures that Λ can be a subset of the partition of the transformed angular coordinates θ^* : each cluster transformation cannot place a vertex closer than $t/2$ to the cluster boundary, which means that there exists an interval of threshold $[t, t + \delta)$ that yields a partition of θ^* containing obtaining Λ for θ^* ($\delta = 0$ if two vertices exactly have a distance of $t/2$ to a cluster boundary, an event of measure zero).

Finally, it's important to note that angular separation between vertices and cluster boundaries changes. This means that the intermediary thresholds are not the same for θ and θ^* and that the interval $[t_{\min}, t_{\max})$ and the intermediary thresholds for θ^* must also be computed in $Q[\Theta^* = \theta|\theta]$.

In summary, each cluster-based subkernel transition is done by first sampling T according to Eq. (C10), which gives a partition \mathcal{C} for the current angular coordinates θ . We then sample $\Lambda \subseteq \mathcal{C}$ with $|\Lambda|$ being the required size for the transformation. We apply the cluster transformation with the outcome probabilities $\mathbb{P}[\Theta^* = \theta^*|\Lambda, \theta]$, which yields θ^* . We accept θ^* as the new state with probability $\alpha(\theta^*, \theta)$ of Eq. (C4). The marginalized probability $Q[\Theta^* = \theta|\theta^*]$ that the sampling drew θ^* is given by Eq. (C5) (and $Q[\Theta^* = \theta|\theta^*]$ is simply obtained by exchanging $\theta \leftrightarrow \theta^*$ in the equations and by using the Λ that was sampled to produce θ^* in the first place).

Appendix D: Convergence diagnostics

Assessing the quality of an MCMC sampler can be challenging. At the very least, one should verify that (1) the autocorrelation of the states decreases with the lag and (2) the stationary distribution is identical no matter the initial state. The former indicates how small the error of Monte Carlo estimators is (Markov chain central limit theorem), and the latter suggests that a Markov chain running long enough will lead to the correct stationary distribution. In this section, we present the effective sample size and the potential scale reduction factor, proxies of these desired properties. We also extend these statistics to random variables on the circle.

The Gelman-Rubin [77] potential scale reduction factor \hat{R} indicates whether or not the different chains “agree” on the typical values of the parameters. Let $(x_1^{(m)}, x_2^{(m)}, \dots, x_N^{(m)})$ be the m^{th} Markov chain's state, and for the sake of simplicity, let us assume that we have M chains of equal length N . The total chain variance is estimated with the weighted average

$$\widehat{\text{var}}^+ := \frac{N-1}{N}W + \frac{1}{N}B, \quad (\text{D1})$$

where W and B/N are, respectively, the within-chain average variance and the between-chain variance

$$W = \frac{1}{M} \sum_{m=1}^M s_m^2, \quad (\text{D2})$$

$$B = \frac{N}{M-1} \sum_{m=1}^M (\bar{x}^{(m)} - \bar{x})^2, \quad (\text{D3})$$

and where s_m^2 and $\bar{x}^{(m)}$ are the sample variance and sample average

$$s_m^2 = \frac{1}{N-1} \sum_{j=1}^N (x_j^{(m)} - \bar{x}^{(m)})^2, \quad (\text{D4})$$

$$\bar{x}^{(m)} = \frac{1}{N} \sum_{j=1}^N x_j^{(m)}, \quad (\text{D5})$$

$$\bar{x} = \frac{1}{M} \sum_{m=1}^M \bar{x}^{(m)}. \quad (\text{D6})$$

The potential scale reduction factor is then

$$\hat{R} := \sqrt{\frac{\widehat{\text{var}}^+}{W}}. \quad (\text{D7})$$

When an MCMC algorithm mixes properly, the chains $\hat{R} \rightarrow 1$ as $N \rightarrow \infty$. We use the “split- \hat{R} ” variant [78], where each chain is split in two for the computation of \hat{R} . This adjustment helps detect a within-chain lack of convergence. Note that having a small \hat{R} is a necessary but insufficient convergence condition.

The effective sample size quantifies how many sample points of the sample are considered independent. The (unnormalized) sample autocovariance is

$$a_m(\tau) = \sum_{j=1}^{N-\tau} (x_j^{(m)} - \bar{x}^{(m)})(x_{j+\tau}^{(m)} - \bar{x}^{(m)}), \quad (\text{D8})$$

The effective sample size of chain m is [79]

$$n_{\text{eff}}^{(m)} \approx \frac{N}{1 + 2 \sum_{\tau=1}^N \rho_m(\tau)} \quad (\text{D9})$$

where $\rho_m(\tau) = a_m(\tau)/a_m(0)$ is the normalized sample autocovariance. In practice, Eq. (D8) is noisy for large τ because there are not enough sample points. We use a maximum lag of $\tau = \lfloor N/50 \rfloor$.

Autocorrelations can be combined across chains using [67]

$$\rho(\tau) = 1 - \frac{W - \frac{1}{M} \sum_{m=1}^M s_m^2 \rho_m(\tau)}{\widehat{\text{var}}^+}, \quad (\text{D10})$$

which yields the global effective sample size

$$N_{\text{eff}} \approx \frac{NM}{1 + 2 \sum_{\tau=1}^N \rho(\tau)}. \quad (\text{D11})$$

We use the same heuristic as $n_{\text{eff}}^{(m)}$ for the maximal lag value.

N_{eff} and \hat{R} statistics are typically used for continuous random variables defined on the real line. Hence, we use these for the parameters κ_u and β . However, they are not appropriate for the angular coordinates because of the cyclic boundary condition. The issue stems from additions and subtractions that appear in averages, Eq. (D11) and Eq. (D7).

To extend S_{eff} and \hat{R} to a Markov chain realization $(\theta_0^{(m)}, \theta_1^{(m)}, \dots, \theta_N^{(m)})$ on the circle, we use the circular analogues of the sample average and the sample correlation coefficient, which are respectively [80]

$$\bar{\phi} := \arg \left(\sum_{j=1}^S \exp\{i\phi_j\} \right), \quad (\text{D12})$$

$$r_{\Phi, \Psi} := \frac{\sum_{j=1}^S \sin(\phi_j - \bar{\phi}) \sin(\psi_j - \bar{\psi})}{\sqrt{\sum_{j=1}^N \sin^2(\phi_j - \bar{\phi})} \sqrt{\sum_{j=1}^N \sin^2(\psi_j - \bar{\psi})}}, \quad (\text{D13})$$

where i is the imaginary number, and $(\phi_j)_{j=1}^S$ and $(\psi_j)_{j=1}^S$ are i.i.d. samples of Φ and Ψ respectively with Φ

and Ψ being random variables on the circle. Note that, to simplify notation, θ_j denotes the j th state of the Markov chain realization instead of the angular coordinate of vertex j .

The circular autocorrelation coefficient at lag τ is obtained directly from Eq. (D13) with the sample points $\phi_j = \theta_j$ and their lagged values $\psi = \theta_{j+\tau}$. Since the numerator is analogous to the (unnormalized) covariance

$$a_o(\tau) = \sum_{j=1}^{N-\tau} \sin(\theta_j - \bar{\theta}) \sin(\theta_{j+\tau} - \bar{\theta}), \quad (\text{D14})$$

we define the normalized autocovariance function

$$\rho_o(\tau) := \frac{a_o(\tau)}{a_o(0)} \quad (\text{D15})$$

that leads to the circular effective sample size

$$n_{\text{eff}}^{\circ} \approx \frac{1}{1 + 2 \sum_{\tau=1}^N \rho_o(\tau)}. \quad (\text{D16})$$

To obtain the circular equivalents of S_{eff} and \hat{R} , we use the circular sample average for \bar{x} and $\bar{x}^{(m)}$ and substitute the subtractions $(\phi - \psi)$ with $\Delta(\phi, \psi)$ in Eqs. (D3) and (D4).

Dataset	$ V $	S_{eff}	Density			Clustering			Global hierarchy level			AUC		
			Original	BIGUE	Mercator	Original	BIGUE	Mercator	BIGUE	Mercator	BIGUE	Mercator		
Macaque	47	341 [306, 523]	0.29	0.28 [0.27, 0.29]	0.29 [0.28, 0.29]	0.55	0.51 [0.50, 0.53]	0.54 [0.53, 0.55]	0.63	0.61, 0.65]	0.63 [—]	0.93	[0.92, 0.93]	0.95 [—]
Zachary	33	1010 [811, 1159]	0.15	0.14 [0.13, 0.15]	0.15 [0.14, 0.15]	0.26	0.30 [0.27, 0.33]	0.31 [0.30, 0.33]	0.53	[0.46, 0.59]	0.80 [—]	0.90	[0.88, 0.91]	0.99 [—]
Critics	29	959 [683, 1154]	0.18	0.17 [0.16, 0.18]	0.13 [0.13, 0.14]	0.17	0.31 [0.28, 0.35]	0.24 [0.20, 0.27]	0.35	[0.31, 0.42]	0.61 [—]	0.80	[0.79, 0.82]	0.91 [—]
Gangs	23	1059 [553, 1152]	0.27	0.26 [0.24, 0.27]	0.27 [0.26, 0.28]	0.36	0.41 [0.39, 0.44]	0.42 [0.40, 0.44]	0.35	[0.32, 0.43]	0.57 [—]	0.90	[0.89, 0.91]	0.96 [—]
Zebras	23	661 [378, 793]	0.42	0.41 [0.40, 0.43]	0.42 [0.41, 0.42]	0.84	0.76 [0.73, 0.79]	0.85 [0.84, 0.87]	0.32	[0.30, 0.35]	0.52 [—]	0.97	[0.97, 0.98]	1.00 [—]
Terrorism	18	1039 [775, 1142]	0.41	0.40 [0.37, 0.41]	0.41 [0.39, 0.41]	0.56	0.55 [0.52, 0.58]	0.58 [0.56, 0.59]	0.47	[0.45, 0.53]	0.56 [—]	0.92	[0.90, 0.93]	0.98 [—]
Kangaroo	16	655 [422, 817]	0.75	0.74 [0.72, 0.75]	0.75 [0.74, 0.75]	0.85	0.84 [0.82, 0.86]	0.85 [0.85, 0.86]	0.24	[0.21, 0.27]	0.26 [—]	0.98	[0.98, 0.99]	1.00 [—]
Tribes	16	962 [521, 1125]	0.48	0.46 [0.41, 0.47]	0.49 [0.47, 0.51]	0.53	0.55 [0.51, 0.59]	0.55 [0.52, 0.58]	0.28	[0.22, 0.32]	0.42 [—]	0.79	[0.76, 0.81]	0.86 [—]

TABLE I. Numerical values of the properties shown in Fig. 6. For each property, the reported values are in order: original, BIGUE, and Mercator. For the effective sample size S_{eff} , the interquartile range is given instead of the highest density interval. Each sample is a combination of 4 chains of length 300. The effective sample size can be greater than the sample size when the autocorrelation is negative on odd lags.